Langmuir

Article

pubs.acs.org/Langmuir

Understanding Morphology-Controlled Synthesis of Zinc Nanoparticles and Their Characteristics of Hydrolysis Reaction

Byoungjun Mun and Donggeun Lee*

School of Mechanical Engineering, Pusan National University, Busan 609-735, South Korea

Supporting Information

ABSTRACT: Two-step thermochemical water-splitting cycle based on a Zn/ZnO redox pair is considered as a potential route for carbon-free production of hydrogen because the first hydrolysis step of the cycle highly depends on the method of preparation and the resultant particle characteristics, such as size, morphology, surface state, and initial oxide content. Here, employing a conventional evaporation and condensation method, we successfully produce three types of Zn nanoparticles ranging from nanorods, mesoporous nanorods with nanospheres on their surfaces, and fully sintered nanocrystals. The achievement in morphology control is realized simply by changing the injection position of the quenching gas. We found that the resultant hydrolysis kinetics is highly dependent on the morphology and porosity of the Zn nanoparticles. Finally, a series of simple mathematical modeling is made in an effort to understand the formation mechanism of Zn nanoparticles.

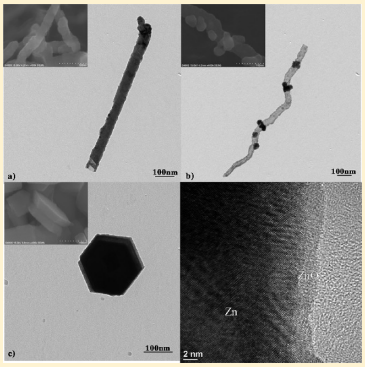

INTRODUCTION

The two-step thermochemical water-splitting cycle based on a Zn/ZnO redox pair has been considered as a potential route for carbon-free production of hydrogen. The cycle involves an exothermic step of Zn hydrolysis to produce hydrogen and ZnO at 300−800 °C (eq 1)[1−8] followed by an endothermic reduction step to convert ZnO to Zn, which is realized at 1600−1750 °C by using concentrated solar energy (eq 2).[9−11]

$$\mathrm{Zn(s) + H_2O \rightarrow ZnO(s) + H_2} \quad (1)$$

$$\mathrm{ZnO(s) \rightarrow Zn(s) + \frac{1}{2}O_2} \quad (2)$$

From thermodynamic and economic analysis, Steinfeld[1] demonstrated that this cycle, if realized on an industrial scale, could be competitive with the electrolysis of water using solar cells. An analogous reaction route has also been demonstrated to work for conversion of CO_2 and H_2O to syngas:[12−14]

$$\mathrm{Zn(s) + \beta CO_2 + (1-\beta)H_2O \rightarrow ZnO(s) + \beta CO + (1-\beta)H_2} \quad (3)$$

In addition, the Zn/ZnO redox pair offers the additional benefits of carbon-free and environmental friendly production of hydrogen as compared to conventional reforming processes of hydrocarbon because hydrogen is the only gas product during the hydrolysis step. Thus, the promising prospect of the cycles in the areas of energy and environment has triggered many investigations.

Though the hydrolysis reaction of eq 1 is thermodynamically favorable below 1400 K,[7] the reaction is kinetically constrained.[7] The hydrolysis reaction has been studied on various forms of Zn materials, such as Zn melt,[12] Zn vapor,[13] solar Zn,[14] and Zn powders.[2] Because the hydrolysis reaction is basically heterogeneous,[7] Zn nanoparticles have been more often tested to promote the reaction kinetics than other coarse materials mainly due to their higher surface to volume ratio. Meanwhile, early studies[3,4,7] at ETH were mainly focused on developing a prototype of a one-step aerosol reactor for in situ formation and hydrolysis of Zn nanoparticles. Despite their successful demonstration, the two processes (formation and hydrolysis) were hardly discriminated in a sort of black box (reactor), which made it difficult to clarify what type of Zn nanoparticle is desirable and why.

More recently, researchers, including the ETH group, chose to separate the two processes and began to study kinetic measurements and the reaction mechanism of hydrolysis using well-known commercial Zn nanoparticles of ∼160 nm[2,5,8] and micrometer size[8] or well-defined Zn nanocrystals of hexagonal-prism shape.[6] Referring to Table 1 in ref 6, one can notice that there are large discrepancies in activation energy of the hydrolysis reaction, which is unlike the reaction order or the mechanism. The big differences in activation energy have been explained by the difference in methods of preparation and the resultant particle characteristics, such as size, morphology, surface state, and initial oxide content.[6]

This turns our attention to developing a simple method to produce various Zn nanoparticles with controlled morphology and to gaining a better understanding of the synthesis process itself. The conventional method of evaporation and nucleation/condensation of metal in an inert gas might be the simplest process in analysis and control because the process (thermally

Received: February 28, 2013
Revised: April 13, 2013
Published: April 29, 2013

   dx.doi.org/10.1021/la400765j | Langmuir 2013, 29, 6174−6180

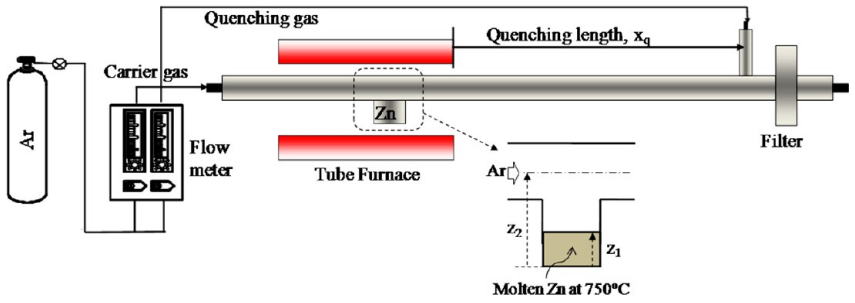

Figure 1. Experimental setup for the synthesis of Zn nanoparticles.

driven) does not accompany any complicated chemical processes, which makes it easy to understand. This method offers additional benefits of easy scale up and no need of a further reduction step. However, it is surprising to find that only a few articles[15,16] are available on the production of Zn nanoparticles under control of morphology via this aerosol method, in contrast to there being a large number of papers dealing with the production of ZnO particles including nanowires and belts (refs 17−20 and their references).

Thus, the goal of this study was to produce Zn nanoparticles with controlled morphologies using a similar evaporation/condensation method and then to perform a series of simple numerical calculations in an attempt to explain the production mechanism of Zn nanoparticles. As a result, simply varying the quenching positions, we could produce a variety of Zn nanoparticles from nanorod to porous nanorod, and fully sintered nanocrystals showing distinct hydrolysis reaction characteristics from commercial Zn particles.

EXPERIMENTAL SECTION

Zn nanoparticles were generated through an evaporation/condensation method in an argon flow, as schematically shown in Figure 1. A stainless-steel (SS) container containing commercial Zn pellets (99% purity, Sigma-Aldrich) was T-connected between two straight $^1/_2$" SS tubes and then placed in the middle of a hot-wall tube furnace (w/30 cm long hot zone). The furnace temperature was kept constant at 750 °C − well above the melting point (419 °C) but below the boiling point (907 °C) of Zn.[21] Thus, the Zn pellets were completely melted and then evaporated. An inert carrier gas of Ar was introduced to the Zn container at a rate of 5 lpm to sweep the Zn vapor out of the hot furnace and it was then slightly cooled. Next, the Zn vapor was quenched by injecting additional Ar gas at 5 lpm at a distance of x_q from the furnace exit (Figure 1). The quenching positions, noted by x_q, were varied to 25, 55, and 85 cm. As such, Zn vapor was highly supersaturated somewhere downstream of the furnace exit and thereby underwent nucleation and self-seeded condensation to convert its form to nanoparticles. As-generated nanoparticles were collected on a glass microfiber filter (25 mm in diameter, Whatman) located 12 cm downstream of the quenching position. Note that those Zn powders, when exposed to natural atmosphere (indoor air), are often oxidized to form a thin ZnO layer on their surface.[5] The as-generated Zn powders were contained in a N_2-filled glass bottle prior to further experiments.

The as-prepared Zn samples were then dispersed in ethanol with an ultrasonicator. A few milliliters of Zn−ethanol suspension were dropped on a SiO_2-coated TEM grid and then dried in a N_2-filled container. The size and morphology of the Zn particles were measured by a transmission electron microscope (TEM; H-7600, Hitachi, 100 kV) equipped with an energy dispersive spectrometer (EDS) and a field-emission scanning electron microscope (FE-SEM; S-4800, Hitachi, 10 kV). The detail microstructures of the Zn nanoparticles were measured by a high-resolution transmission electron microscope (HR-TEM; 2100F, JEOL, 200 kV) sometimes together with a selected area electron diffraction (SAED) mode. Lattice spacing of particles was measured from HRTEM images and compared with the JCPDS database to identify crystalline parts. The specific surface area, pore size, and volume of the particles were measured by a gas sorptometer (Autosorb-1, Quantachrome) using nitrogen adsorption at 77 K and Brunauer−Emmett−Teller (BET) analysis.[22] X-ray Diffraction (XRD, D/MAX-2400, Rigaku) was used to analyze the mole content of ZnO in the Zn particles before and after their hydrolysis reaction.[23−25] The XRD measurement was performed by scanning the angle of 2θ in the range of 30−60° at a rate of 6° min^{-1} while irradiating Cu Kα X-ray (30 kV, 40 mA, 0.15218 nm). A dynamic thermogravimetric analysis (TGA; Q50, TA Instruments) was done for the Zn samples to investigate the hydrolysis reaction kinetics in such a way that 5 mg of Zn nanoparticles was heated at 10 °C min^{-1} with a flowing steam/Ar mixture gas at 60 ccm.[26] The steam of ∼23 vol % was supplied by passing the Ar gas though a bubbler containing liquid water. Any remaining atmosphere inside the TGA was swept by flowing Ar gas for an hour prior to every TGA experiment. As such, considerable efforts were made to keep a minimal but consistent exposure of the samples to air in preparation for the characterization experiments. The total exposure time was less than 1 h. More details on characterization experiments were described elsewhere.[22−26]

RESULTS AND DISCUSSION

Characteristics of As-Prepared Zn Nanoparticles. Figure 2 shows TEM images of Zn particles collected three different positions, x_q = 25, 55, and 85 cm. The inset of each figure denotes a corresponding SEM image to show 3D morphology. At x_q = 25 cm, given the shortest residence time of ∼0.28 s until being collected, the as-generated Zn particles are almost 1D nanorods that are 40−80 nm thick and 400−1000 nm long. The aspect ratio of the nanorods ranges from 10 to 15. BET analysis reveals that the Zn nanorods have a specific surface area of 146 m^2 g^{-1}, which is almost 15 times higher than the value of solid (nonporous) equivalent nanorods. The cumulative pore size distribution (as shown in Figure S1 of the Supporting Information) clearly indicates that the Zn nanorods are indeed microporous with a mean pore size of 3.6 nm.

Zn particles collected at x_q = 55 cm look alike except for the fact that the nanorods are a little more curvy with many spherical dots on the surface. Because the particles look like budded twigs, they are called budded nanorods hereafter. The nanorods have a similar diameter and a little longer length as compared to the first case, whereas the spherical dots are 20−60 nm in diameter. BET analysis reveals that the specific surface area of the particles is as large as 527 m^2 g^{-1} together with a larger pore size (∼10 nm) suggesting that the budded nanorods are mesoporous. This is confirmed by the pore size distribution seen in Figure S1 of the Supporting Information. Unlike these cases, the particles collected at x_q = 85 cm are quite different in morphology: hexagonal prismlike nanocrystals, as shown in part c of Figure 2, probably resulting from complete sintering for the

dx.doi.org/10.1021/la400765j | Langmuir 2013, 29, 6174−6180

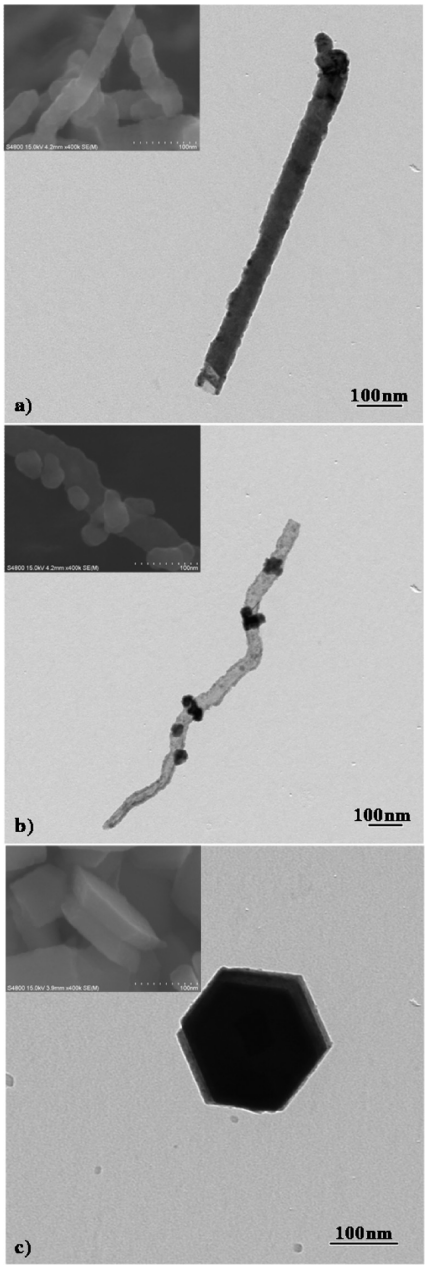

Figure 2. TEM images of as-generated Zn nanoparticles (a) nanorods obtained at x_q = 25 cm, (b) budded nanorods at x_q = 55 cm, (c) nanocrystals at x_q = 85 cm. The inset of each image shows 3D SEM images.

longest residence time. The nanocrystals appear very similar to Ma et al.'s[15] nanocrystals in size and shape. The present nanocrystals are shown to not be porous by BET measurement.

HR-TEM imaging reveals that the three kinds of Zn nanoparticles are all covered with 2−3 nm thick ZnO layers. An example is shown in Figure S2 of the Supporting Information; the Zn nanorods at x_q = 25 cm are ∼55 nm in diameter with clear evidence of lattice fringes especially in the Zn core part. With the sizes and densities (ρ_{Zn} = 7140 kg m^{-3}, ρ_{ZnO} = 5600 kg m^{-3}) of Zn and ZnO, the weight percent of ZnO in the Zn nanorods is ca. 13%. As reported by Ernst et al.,[5] Zn nanoparticles are readily oxidized by exposure to indoor air and the resultant ZnO layer plays an important role in the hydrolysis reaction kinetics. Hence, it is important to indentify the ZnO content for the three types of particles.

Referring to eq 1, complete hydrolysis of pure Zn to ZnO leads to a mass increase of 24.6%. Because TGA measures the initial and final sample masses (denoting w_i and w_f, respectively) for complete hydrolysis of the Zn/ZnO sample, such TGA experiments are useful in estimating the unknown mass ($w_{i,ZnO}$) of the ZnO layer of the sample as

$$1.246 = \frac{w_f - w_{i,ZnO}}{w_i - w_{i,ZnO}} \quad (4)$$

This process is repeated for the three kinds of Zn particles, each of which has been exposed to indoor air for <1 and 12 h. The results are summarized in Table 1. The ZnO content of all

Table 1. Weight Percents of ZnO Layer of As-Received Zn Nanoparticles Collected at Three Different Positions after Being Exposed to Indoor Air for Two Different Times

	$w_{i,ZnO}/w_i$		
time	at 25 cm	at 55 cm	at 85 cm
10 min	13.9%	16.3%	10.7%
12 h	17.5%	25.6%	11.8%

samples clearly increase with an increasing exposure time, indicating the oxidation effect, though the second sample at 55 cm turns out to be the most sensitive and reactive to exposure, whereas the nanorods at 25 cm are the second most sensitive. It is of interest to note that the order of sensitivity of the samples is exactly consistent with that of the sample porosity measured by BET. Moreover, the weight percent of the nanorods (at 25 cm for <1 h exposure) is in good agreement with the value (13%) obtained from TEM analysis.

It is worth noting that the estimation method for the value of $w_{i,ZnO}$ can be justified only upon complete hydrolysis of the sample. To confirm the hydrolysis completion, XRD was used on the sample after exposure to steam in the TGA. Figure S3 of the Supporting Information shows XRD profiles of the three samples before and after hydrolysis reaction and part b of Figure S3 of the Supporting Information indicates clearly that there are no Zn peaks and only ZnO peaks. In part b of Supporting Information, as the peak of ZnO at 2θ = 31.9° is ∼70% as large as its biggest peak at 36.4° and not overlapped with any XRD peak of Zn, it would be used as a marker to estimate the initial fraction of ZnO in the samples. In part a of Figure S3 of the Supporting Information, a hidden ZnO peak at 36.4°, which is only 140% as large as the very little peak of ZnO at 31.9°, is overwhelmed by the second largest peak of Zn. Peak deconvolution analysis[23−25] revealed that the biggest peak height of ZnO is only 1.8% of that of the Zn suggesting that crystalline ZnO content is ∼2.3 wt % in the original sample. The larger ZnO content given in Table 1 indicates that the ZnO mainly exists in an amorphous form.

Hydrolysis Reaction of Zn Nanoparticles. TGA curves for the hydrolysis reaction of the three types of Zn nanoparticles are shown in Figure 3 where the vertical axis represents the relative mass increase of the Zn core excluding the oxide layer in a similar way to eq 4. The hydrolysis reaction for Zn nanorods and budded nanorods start at 100 °C and terminate at ∼460 °C, which is much faster than others (nanocrystals and commercial samples). The reaction of nanocrystals appears to be distinctively delayed as much as

dx.doi.org/10.1021/la400765j | Langmuir 2013, 29, 6174−6180

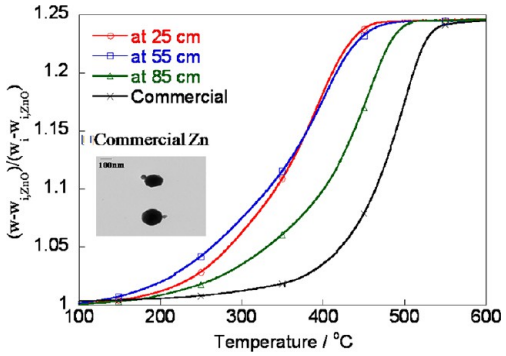

Figure 3. TGA curves of the three types of Zn nanoparticles and commercial Zn nanopowder. The y axis represents a relative mass increase of the core part of Zn; w, w_i, and $w_{i,ZnO}$ correspond to the sample mass, the initial sample mass, and the initial mass of the ZnO layer, respectively.

50 °C, whereas the commercial nonporous Zn spherical particles shown in the inset of Figure 3 exhibit the slowest hydrolysis reaction among them. Such a distinct enhancement in reactivity for the first two samples is attributed to the porous structure of the samples (recall the BET results) enabling easy access to the reacting gas/vapor. It is also interesting to note that the budded nanorods exhibit higher reactivity than the nanorods below 350 °C. Their enhanced low-temperature reactivity might be explained by the BET observation that the budded nanorods are mesoporous with the largest surface area. This postulation is also supported by Table 1 where the room-temperature oxidation for 12 h was likewise the most significant in the budded nanorods. The fractional conversion of Zn (α) for each sample was extracted at 200 and 250 °C from Figure 3 and plotted against specific surface area (SSA) of the sample. Figure S4 of the Supporting Information clearly showed that the SSA or surface state obviously influenced the hydrolysis reaction and the resultant conversion α suggesting that the hydrolysis is a sort of surface limited reactions especially at low temperatures.

There remains another question to clarify: why nonporous nanocrystals are more reactive than the commercial sample with a similar size? The answer seems to lie in the morphology difference between the samples. Ma and his colleagues recently reported experimental evidence of anisotropic (crystal-face-dependent) evaporation[15] and oxidation[27] of hexagonal-prism-shaped Zn nanocrystals of ~100 nm. Evaporation and oxidation took place preferentially on the side wall and edges of the hexagonal prism where the surface energy was expected to concentrate due to their lower coordination numbers rather than the top and bottom surfaces. From the analogy between hydrolysis and oxidation, it is therefore reasonable to postulate that our nanocrystals that have such sharp edges exhibit enhanced reactivity compared to spherical commercial particles.

Moreover, to investigate the reaction mechanism, morphological changes of our three types of Zn particles during the hydrolysis were monitored as follows. A representative single Zn particle prepared on a TEM grid was chosen to take a picture of. Examples are seen in the left column of parts a1, b1, and c1 of Figure 4 corresponding to a Zn nanorod, budded nanorod, nanocrystal, respectively, before hydrolysis. The particle-containing TEM grid was then heated in a similar way for the present TGA experiment and the same, but hydrolyzed, particle was found again to take another picture of. The corresponding three pictures are shown in the right column of Figure 4. Interestingly, the nanorod turns out to be a hollow nanorod after the hydrolysis completion, whereas the budded nanorod does not despite their seemingly similar morphology. Loutzenhiser et al.[28] and Stamatiou et al.[29] reported that hollow ZnO particles formed from the reaction of Zn particles with H_2O/CO_2 and CO_2, respectively, especially when the gases react primarily on the particle surface (that is, particles are less porous). The mechanism[28] they proposed was as follows. First, the surface reaction resulted in the formation of a ZnO layer on the pristine particle surface (Zn) leading to core−shell structures. Whereas the reaction proceeded further, the ZnO layer became thickened and strengthened enough to resist the shrinking (and denser) Zn core leaving the pore inside the shell. However, this was apparently not the case for the budded nanorod with larger pores, probably allowing the reaction to occur throughout the entire sample, as is seen in parts b1 and b2 of Figure 4. The sharp edges of the nanocrystal in part c1 of Figure 4 became blurred along with hollow inner structure after the hydrolysis, which looks consistent with in parts a1 and a2 of Figure 4.

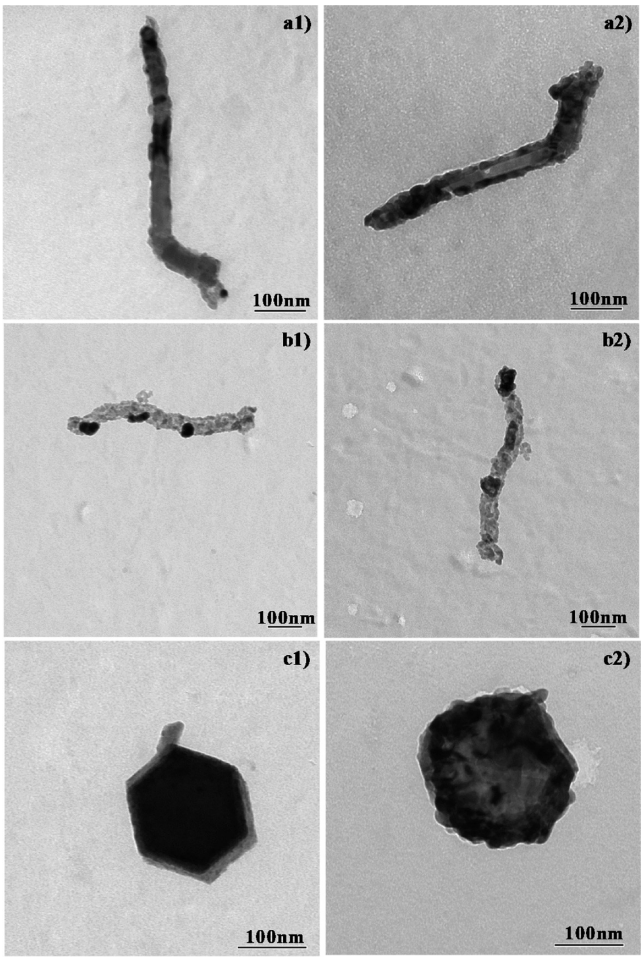

Figure 4. Morphology changes of the three types of Zn nanoparticles denoting (a) nanorods, (b) budded nanorods, and (c) nanocrystals during the hydrolysis. Three images in the left column represent pristine particles before hydrolysis, whereas the images in the right column show the results after hydrolysis completion.

Formation Mechanism of Zn Nanoparticles. It is no doubt of great interest that our simple method is quite successful in controlling the morphology and resultant reactivity of Zn nanoparticles with one step. Thus, better

dx.doi.org/10.1021/la400765j | Langmuir 2013, 29, 6174−6180

understanding of the method and mechanism should be helpful at this point. As the phenomenon is apparently simple, that is, evaporation, nucleation, and condensation of Zn, let us start from the evaporation. Bulk Zn evaporates above its melting point of 419 °C. The rate of Zn evaporation ($\dot{m}_{evap}$) from a container (enlarged drawing in Figure 1) is calculated by[30]

$$\dot{m}_{evap} = A\frac{cD_{AB}}{z_2 - z_1}\ln\frac{1 - y_{Zn2}}{1 - y_{Zn1}} \quad (5)$$

where c is the total mole concentration (11.8 mol m^{-3} given from ideal gas law at 1023 K) and D_{AB} is the diffusivity of Zn vapor obtained by Chapman−Enskog formula as

$$D_{AB} = \frac{0.00186T^{3/2}\left[\frac{1}{M_{Zn}} + \frac{1}{M_{Ar}}\right]^{1/2}}{P_t\sigma_{AB}^2\Omega_D} \quad (6)$$

where T is the temperature in units of K, M_{Zn} and M_{Ar} are the molecular weights of Zn and Ar in units of g mol^{-1}, P_t is the total pressure of 1 atm, σ_{AB} is an the arithmetic average of the mean molecular diameters of the two gases, Ar and Zn vapor[31] in the present case (=($\sigma_{Zn} + \sigma_{Ar}$)/2 = 2.77 Å), and Ω_D, the diffusion collision integral,[30] is estimated as 1.05. Using those values, the D_{AB} is obtained as 1.31 cm^2 s^{-1} at the present condition. Again in eq 5, $z_2 - z_1$ is the diffusion distance of evaporating Zn vapor from the surface of molten Zn (z_1) to Ar gas flow (z_2) as seen in Figure 1. The mean value of $z_2 - z_1$ is measured at 12.5 mm, whereas the top surface area (A) of the Zn melt is 83.3 mm^2. The terms of y_{Zn1} and y_{Zn2} represent the mole fractions of Zn vapor at the positions of z_1 and z_2, respectively. The y_{Zn2} was set to zero under the assumption of complete removal of Zn vapors by a high-speed Ar flow, whereas the y_{Zn1} is calculated at 0.558 by the ratio of the saturation vapor pressure of Zn[32,33] at 1023 K to the total pressure P_t. Thus, the evaporation rate is estimated at ∼8.4 × 10^{-6} mol s^{-1}. On the basis of this rate relative to the Ar flow rate, the partial pressure of Zn vapor (P_{Zn}) near the reactor exit is calculated to be ∼251 Pa. This is the starting point of the following analysis.

The Zn vapor carried by Ar gas is gradually cooled down leading to a significant decrease in the saturation vapor pressure of Zn ($P_{Zn,sat}$)[33] with respect to the invariant P_{Zn} and thereby making the vapor supersaturated. The degree of supersaturation becomes much more significant by the quenching, which drops the temperature, possibly inducing nucleation of the Zn particles. In this respect, gas temperatures are measured along the tube axis in such a way that a K-type thermocouple is inserted from the tube exit to different positions (x_q). The temperatures are measured twice, that is, with and without quenching for each case. Figure 5 shows axial variations of P_{Zn}, $P_{Zn,sat}$, and temperatures with and without quenching for the three cases, x_q = 25, 55, and 85 cm. The x axis represent the distance from the furnace exit. The square and circle symbols denote experimental data.

Classical nucleation theory was applied to estimate the nucleation rate (J) of Zn seeds as large as Kelvin diameter, the minimum size of stable nuclei, as[34]

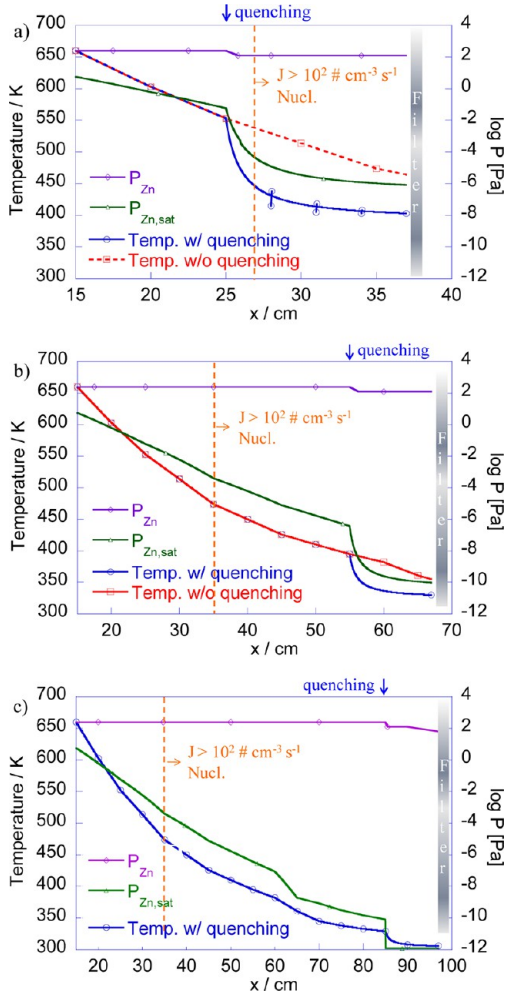

Figure 5. Variations of temperature with and without quenching, partial pressure (P_{Zn}), and saturation vapor pressure of Zn vapor ($P_{Zn,sat}$) along the tube axis, for three different quenching positions (a) at 25 cm, (b) at 55 cm, (c) at 85 cm.

$$J = \frac{P_{Zn}}{(2\pi m_{Zn}k_BT)^{1/2}}\frac{2v_{Zn}\sigma_{Zn}^{1/2}}{(k_BT)^{1/2}}N_{Zn} \times \exp\left[-\frac{16\pi}{3}\frac{v_{Zn}^2\sigma_{Zn}^3}{(k_BT)^3(\ln S)^2}\right][\#\ \mathrm{cm}^{-3}\ \mathrm{s}^{-1}] \quad (7)$$

where the molecular mass (m_{Zn}) is 1.09 × 10^{-22} g molecule^{-1}, and the molecular volume (v_{Zn}) is obtained from the density (ρ_{Zn}):[35] ρ_{Zn} = 6.575 − 1.1 × 10^{-3} (T − 692) in units of g cm^{-3}, the surface tension of Zn is given by[35] σ_{Zn} = 782 − 0.17 (T − 692) in units of mN m^{-1}, the supersaturation ratio (S) is the ratio of P_{Zn} to $P_{Zn,sat}$: log($P_{Zn,sat}$) = −7198/T + 9.664 in units of mmHg,[33] T is in K and the molecular number density (N_{Zn}) in units of # cm^{-3} is given from the ideal gas law. The P_{Zn} is corrected for quenching-gas dilution and consumptions for nucleation and condensation.

Again in Figure 5, it is noted that the pressures of P_{Zn} and $P_{Zn,sat}$ are plotted at log scale (right-hand side). The P_{Zn} is shown to decrease mainly due to the quenching but certainly not so much as the $P_{Zn,sat}$ does. A brown vertical line in parts a−c of Figure 5 denotes the position at which the value of J reaches 10^2 # cm^{-3} s^{-1} as the nucleation starting position. For the case of x_q = 25 cm (part a of Figure 5), the nucleation is

dx.doi.org/10.1021/la400765j | Langmuir 2013, 29, 6174−6180

clearly induced by the quenching and starts at x = 27 cm, whereas in the other two cases highly supersaturated Zn vapor becomes self-nucleated at ~35 cm due to natural cooling even prior to the quenching. This is why the nucleation position is almost the same and not affected by the quenching in the latter cases. Further downstream, the nucleation rate rapidly increases up to 1.3×10^5, 8.5×10^7, and 2.0×10^9 # cm^{-3} s^{-1} for x_q = 25, 55, and 85 cm, respectively. The residence time of nuclei until filtration is 0.057, 0.34, and 0.74 s in the order of the three cases.

Here, the nuclei can grow by either interparticle coagulation or vapor condensation on the nuclei surface. To make a decision on the growth mechanism, the characteristic collision time of nuclei (τ_{CF}) in the free molecular regime is estimated by[34]

$$\tau_{CF} = \frac{1}{(3\phi/4\pi)^{1/6}(6k_BT/\rho_{Zn})N_0^{5/6}} \quad (8)$$

where ϕ and N_0 are the volume fraction and number density of the total particles at a certain position of x; the N_0 is obtained by numerical integration of the J over the residence time to x. Though the τ_{CF} is the shortest in the third case, x_q = 85 cm, where the N_0 and ϕ are maximum, the minimal τ_{CF} is ~80 s, much longer than the residence time. Note that the condensational growth of nuclei was not considered for simplicity in the calculation resulting in the upper limit of N_0 and the lower limit of τ_{CF}; if considered, the vapor condensation reduces P_{Zn}, S, J, and finally N_0. Thus, the results finally suggest that those Zn particles seen in Figure 2 result mainly from the nucleation and condensation. To double check this inference, the condensational growth rate of the single nucleus is calculated as[34]

$$\frac{dd_p}{dt} = \frac{2\alpha_s(P_{Zn} - P_{Zn,sat})v_{Zn}}{(2\pi m_{Zn}k_BT)^{1/2}} \quad (9)$$

where d_p is the diameter of a particle growing from its Kelvin diameter and α_s is the sticking coefficient[36] that is assumed to unity here. For the first case of x_q = 25 cm, the growth rate is ca. 6.1×10^4 nm s^{-1} at the nucleation position corresponding to a ~150 nm growth in diameter during the traveling from x = 27 to 28 cm (for ~2.5 ms). Thus, the vapor condensation occurs fast enough to make the nucleus grow to a 40−80 nm thick and 400−1000 nm long nanorod. There still remains a question for the 1D growth of the nuclei toward the nanorods. In contrast to the reports of a large number of articles on site-specific growth of ZnO nanowires and nanobelts,[17,18,37−39] there are only a few reports on the synthesis of Zn nanowires.[16,40] Peng et al.[16] and Wang et al.[40] presumed that the unidirectional flow of Zn vapors driven by the carrier gas might cause the preferential 1D growth of Zn nanowires and nanobelts. As demonstrated by Ma and his colleagues, there exist crystallographic site preferences for evaporation[15] and oxidation[27] of Zn nanoparticles. Accounting for the analogy of condensation with evaporation, it is natural to presume that the condensational growth occurs at least anisotropically. Though the two explanations sound plausible, we are not in a position to give a certain answer.

For the second case, the growth rate is almost doubled to 1.19×10^5 nm s^{-1} at the nucleation position. It is reasonable to speculate that Zn atoms accumulating on the particle surface have relatively insufficient time to restructure to high density, making the budded nanorods more porous with larger pore sizes than in the first case, which is consistent with our BET results. The porous nanorods floating further downstream experience a higher rate of vapor condensation, which might facilitate formation of spherical seeds on their surface (just like buds from a branch) as seen in part b of Figure 2. A similar phenomenon has been observed in case of ZnO nanorods: other nanorods can grow directly from a preexisting nanorod, leading to dendritic (branches) structures,[37] which is indicative of the formation of seeds on the ZnO nanorods as a prerequisite.[18] For the third case, all the Zn nanoparticles seem to have enough time to be fully sintered into the hexagonal nanocrystals regardless of their initial morphology.

CONCLUSIONS

In this study, three types of Zn nanoparticles were produced via evaporation and condensation of Zn. Their morphology was successfully controlled simply by changing the injection position of the quenching gas. The first type of sample, obtained at the shortest quenching distance, was microporous nanorods exhibiting excellent hydrolysis kinetics. The second type obtained at an intermediate quenching distance was mesoporous nanorods with spherical nanodots (buds) on their surface. The sample had the largest specific surface area of ~527 m^2 g^{-1} among all of the samples and revealed the most enhanced low-temperature reactivity. The third sample obtained for the longest residence time was fully sintered hexagonal-prismlike nanocrystals, which considerably retarded the hydrolysis reaction. However, their reactivity was still better than a commercial sample of similar size, which was explained by the anisotropic nature of our nanocrystals. A series of simple mathematical modelingwas made in an effort to understand the formation mechanism of the Zn nanoparticles. As a result, the Zn nanorods began to nucleate 2 cm downstream of the quenching position and epitaxially grew via condensation of supersatrurated Zn vapor. In contrast, the nucleation of the budded nanorods commenced via natural cooling even prior to quenching and the subsequent condensation occurred at a doubled rate presumably resulting in more porous and budded structures. The third nanocrystals were believed to result from sintering of nanoparticles.

ASSOCIATED CONTENT

Supporting Information

Pore size distribution of nanorods and budded nanorods, HR-TEM images of the nanorods, XRD patterns of pristine samples and hydrolyzed samples in TGA, correlation of Zn conversion with specific surface area. This material is available free of charge via the Internet at http://pubs.acs.org.

AUTHOR INFORMATION

Corresponding Author

*E-mail: donglee@pusan.ac.kr.

Notes

The authors declare no competing financial interest.

ACKNOWLEDGMENTS

This work was supported by the National Research Foundation of Korea (NRF) grants funded by the Korean government (MEST) (No. 2012-0008830) and also supported by the Global Frontier R&D Program on Center for Multiscale Energy System funded by the National Research Foundation under the

Ministry of Science, ICT & Future, Korea (No. 2012M3A6A7054863).

REFERENCES

(1) Steinfeld, A. Solar hydrogen production via a two-step water-splitting thermochemical cycle based on Zn/ZnO redox reactions. *Int. J. Hydrogen Energy* **2002**, *27*, 611−619.

(2) Funke, H. H.; Diaz, H.; Liang, X.; Carney, C. S.; Weimer, A. W.; Li, P. Hydrogen generation by hydrolysis of zinc powder aerosol. *Int. J. Hydrogen Energy* **2008**, *33*, 1127−1134.

(3) Ernst, F. O.; Tricoli, A.; Pratsinis, S. E.; Steinfeld, A. Co-synthesis of H_2 and ZnO by in-situ Zn aerosol formation and hydrolysis. *AIChE J.* **2006**, *52*, 3297−3303.

(4) Weiss, R. J.; Ly, H. C.; Wegner, K.; Pratsinis, S. E.; Steinfeld, A. H_2 production by Zn hydrolysis in a hot-wall aerosol reactor. *AIChE J.* **2005**, *51*, 1966−1970.

(5) Ernst, F. O.; Steinfeld, A.; Pratsinis, S. E. Hydrolysis rate of submicron Zn particles for solar H_2 synthesis. *Int. J. Hydrogen Energy* **2009**, *34*, 1166−1175.

(6) Ma, X.; Zachariah, M. R. Size-resolved kinetics of Zn nanocrystal hydrolysis for hydrogen generation. *Int. J. Hydrogen Energy* **2010**, *35*, 2268−2277.

(7) Wegner, K.; Ly, H. C.; Weiss, R. J.; Pratsinis, S. E.; Steinfeld, A. In situ formation and hydrolysis of Zn nanoparticles for H_2 production by the 2-step ZnO/Zn water-splitting thermochemical cycle. *Int. J. Hydrogen Energy* **2006**, *31*, 55−61.

(8) Lv, M.; Zhou, J.; Yang, W.; Cen, K. Thermogravimetric analysis of the hydrolysis of zinc particles. *Int. J. Hydrogen Energy* **2010**, *35*, 2617−2621.

(9) Perkins, C.; Lichty, P. R.; Weimer, A. W. Thermal ZnO dissociation in a rapid aerosol reactor as part of a solar hydrogen production cycle. *Int. J. Hydrogen Energy* **2008**, *33*, 499−510.

(10) Schunk, L.; Haeberling, P.; Wepf, S.; Wuillemin, D.; Meier, A.; Steinfeld, A. *J. Sol. Energy Eng.* **2008**, *130*, 021009.

(11) Schunk, L.; Lipinski, W.; Steinfeld, A. Heat transfer model of a solar receiver-reactor for the thermal dissociation of ZnO—Experimental validation at 10kW and scale-up to 1MW. *Chem. Eng. J.* **2009**, *150*, 502−508.

(12) Berman, A.; Epstein, M. The kinetics of hydrogen production in the oxidation of liquid zinc with water vapor. *Int. J. Hydrogen Energy* **2000**, *25*, 957−967.

(13) Melchior, T.; Piatkowski, N.; Seinfeld, A. H_2 production by steam-quenching of Zn vapor in a hot-wall aerosol flow reactor. *Chem. Eng. Sci.* **2009**, *64*, 1095−1101.

(14) Chambon, M.; Abanads, S.; Flamant, G. Kinetic investigation of hydrogen generation from hydrolysis of SnO and Zn solar nano-powders. *Int. J. Hydrogen Energy* **2009**, *34*, 5326−5336.

(15) Ma, X.; Lall, A. A.; Mullholland, G. W.; Zachariah, M. R. Evaporation anisotropy of free nanocrystals. *J. Phys. Chem. C* **2011**, *115*, 16941−16946.

(16) Peng, X. S.; Zhang, L. D.; Meng, G. W.; Yuan, X. Y.; Lin, Y.; Tian, Y. T. Synthesis of Zn nanofibres through simple thermal vapour-phase deposition. *J. Phys. D: Appl. Phys.* **2003**, *36*, L35−L38.

(17) Yuvaraj, D.; Rao, K. N.; Nanda, K. K. Room temperature synthesis of ZnO nanoneedles by activated reactive evaporation. *J. Phys. D: Appl. Phys.* **2009**, *42*, 035403.

(18) Jeong, J. S.; Lee, J. Y. Investigation of initial growth of ZnO nanowires and their growth mechanism. *Nanotechnology* **2010**, *21*, 475603.

(19) Li, J.; Zhang, Q.; Peng, H.; Everitt, H. O.; Qin, L.; Lui, J. Diameter-controlled vapor-solid epitaxial growth and properties of aligned ZnO nanowire arrays. *J. Phys. Chem. C* **2009**, *113*, 3950−3954.

(20) Wang, Y. G.; Sakurai, M.; Aono, M. Mass production of ZnO nanotetrapods by a flowing gas phase reaction method. *Nanotechnology* **2008**, *19*, 245610.

(21) http://www.webelements.com/zinc

(22) Lee, S. G.; Choi, S. M.; Lee, D. The Role of salt in nanoparticle generation by salt-assisted aerosol method: microstructural changes. *Thermochim. Acta* **2007**, *455*, 138−147.

(23) Firmansyah, D. A.; Sullivan, K.; Lee, K. S.; Kim, Y. H.; Zahaf, R.; Zachariah, M. R.; Lee, D. Microstructural behavior of the alumina shell and aluminum core before and after melting of aluminum nanoparticles. *J. Phys. Chem. C* **2012**, *116*, 404−411.

(24) Firmansyah, D. A.; Kim, S.-G.; Lee, K.-S.; Zahaf, R.; Kim, Y. H.; Lee, D. Microstructure-controlled aerosol-gel synthesis of ZnO quantum dots dispersed in SiO_2 nanospheres. *Langmuir* **2012**, *28*, 2890−2896.

(25) Firmansyah, D. A.; Kim, T.; Kim, S.; Sullivan, K.; Zachariah, M. R.; Lee, D. Crystalline phase reduction of cuprous oxide (Cu_2O) nanoparticles accompanied by a morphology change during ethanol-assisted spray pyrolysis. *Langmuir* **2009**, *25*, 7063−7071.

(26) Kim, Y. H.; Kim, Y. -T.; Kim, S. H.; Lee, D. Catalytic oxidation kinetics of iron-containing carbon particles generated by spraying ferrocene-mixed diesel fuel into hydrogen-air diffusion flame. *Carbon* **2010**, *48*, 2072−2084.

(27) Ma, X.; Zachariah, M. R. Oxidation anisotropy and size-dependent reaction kinetics of zinc nanocrystals. *J. Phys. Chem. C* **2009**, *113*, 14644−14650.

(28) Loutzenhiser, P. G.; Galvez, M. E.; Hischier, I.; Stamtiou, A.; Frei, A.; Steinfeld, A. CO_2 splitting via two-step solar thermochemical cycles with Zn/ZnO and FeO/Fe_3O_4 redox reactions II: Kinetic analysis. *Energy Fuels* **2009**, *23*, 2832−2839.

(29) Stamatiou, A.; Loutzenhiser, P. G.; Steinfeld, A. Solar syngas production from H_2O and CO_2 via two-step thermochemical cycles based on Zn/ZnO and FeO/Fe_3O_4 redox reactions: Kinetic analysis. *Energy Fuels* **2010**, *24*, 2716−2722.

(30) Middleman, S. *An Introduction to Mass and Heat Transfer*; John Wiley & Sons, Inc: New York, 1998.

(31) Romer, F.; Kraska, T. Homogeneous nucleation and growth in supersaturated zinc vapor investigated by molecular dynamics simulation. *J. Chem. Phys.* **2007**, *127*, 234509.

(32) Klimova, A. M.; Ananichev, V. A.; Arif, M.; Blinov, L. N. Investigation of the saturated vapor pressure of zinc, selenium, and zinc selenide. *Glass Phys. Chem.* **2005**, *31*, 760−762.

(33) McKinley, J. D.; Vance, J. E. The vapor pressure of zinc between 150° and 350°C. *J. Chem. Phys.* **1954**, *22*, 1120.

(34) Kodas, T. T.; Hampden-Smith, M. J. *Aerosol Processing of Materials*; Wiley-VCH: Canada, 1999.

(35) Brandes, E. A.; Brook, G. B. *Smithells Metals Reference Book*; Butterworth-Heinemann: Oxford, 1992.

(36) Kim, S.; Lee, K.-S.; Zachariah, M. R.; Lee, D. Three dimensional off-lattice Monte Carlo simulations on a direct relation between experimental parameters and fractal dimension of colloidal aggregates. *J. Colloid Interface Sci.* **2010**, *344*, 353−361.

(37) Fan, H. J.; Scholz, R.; Kolb, F. M.; Zachariah, M. Two-dimensional dendritic ZnO nanowires from oxidation of Zn microcrstals. *Appl. Phys. Lett.* **2004**, *85*, 4142−4144.

(38) Law, J. B. K.; Boothroyd, C. B.; Thong, J. T. L. Site-specific growth of ZnO nanowires from patterned Zn via compatible semiconductor processing. *J. Cryst. Growth* **2008**, *310*, 2485−2492.

(39) Cui, S.; Mattson, E. C.; Lu, G.; Hirschmugl, C.; Gajdardziska-Josifovska, M.; Chen, J. Tailoring nanomaterial products through electrode material and oxygen partial pressure in a mini-arc plasma reactor. *J. Nanoparticle Res.* **2012**, *14* (3), 744.

(40) Wang, Y.; Zhang, L.; Meng, G.; Liang, C.; Wang, G.; Sun, S. Zn nanobelts: a new quasi one-dimensional metal nanostructure. *Chem. Commun.* **2001**, 2632−2633.